Key Points:
- We have separately investigated the roles of substorm injection and solar wind pressure in exciting EMIC wave with time-modified AE^+ and $Pd+$
- The source region of EMIC waves driven by large AE^+ is located in the dusk sector and near the magnetic equator
- Large $Pd+$ can solely cause EMIC wave excitation, which has two source regions: near the magnetic equator and in the higher-latitude regions

Correspondence to:
X. Gao and Q. Lu,
gaoxl@mail.ustc.edu.cn;
qmlu@ustc.edu.cn

Statistical Evidence for EMIC Wave Excitation Driven by Substorm Injection and Enhanced Solar Wind Pressure in the Earth's Magnetosphere: Two Different EMIC Wave Sources

Huayue Chen[1,2] (iD), **Xinliang Gao**[1,2] (iD), **Quanming Lu**[1,2] (iD), **Bruce T. Tsurutani**[3] (iD), and **Shui Wang**[1,2]

[1]CAS Key Laboratory of Geoscience Environment, School of Earth and Space Sciences, University of Science and Technology of China, Hefei, China, [2]CAS Center for Excellence in Comparative Planetology, Hefei, China, [3]Retired, Pasadena, CA, USA

Abstract Substorm injection and solar wind dynamic pressure have long been considered as two main drivers of electromagnetic ion cyclotron (EMIC) wave excitation, but clear observational evidence is still lacking. With Van Allen Probes data from 2012–2017, we have investigated the roles of the two EMIC wave drivers separately, by using time-modified AE^+ and P_d^+. Both the occurrence rate and magnetic amplitude of waves significantly increase with the enhancement of each index. During large AE^+, EMIC waves are mainly generated in the dusk sector ($16 \leq$ MLT ≤ 20) and near the magnetic equator ($|$MLAT$| < 10°$). This is presumably due to substorm-injected protons drifting from midnight sector to the plasmaspheric bulge. While during large P_d^+, EMIC waves mainly occur in the noon sector ($9 \leq$ MLT ≤ 15). But there exist higher-latitude ($10° < |$MLAT$| < 20°$) source regions besides equatorial source, possibly due to the minimum B regions. Our results provide strong observational support to existing generation mechanisms of EMIC waves in the Earth's magnetosphere.

Plain Language Summary Electromagnetic ion cyclotron (EMIC) waves are natural emissions in the Earth's magnetosphere, which are believed to be responsible for ion dynamics in the ring current and the loss of relativistic electrons in the radiation belts. How to excite these waves has attracted much attention. In the literature, there exist two potential drivers to excite EMIC waves, such as substorm injection (AE) and solar wind dynamic pressure (P_d). Although previous studies have shown that EMIC waves are closely correlated with AE and P_d, the observational evidence is still needed to confirm these two scenarios of wave excitation. In this study, we have developed a new technique to separately investigate the effects of each driver for EMIC wave generation, with time-modified AE^+ and P_d^+. First of all, either strong substorm injection or solar wind pressure can individually cause the generation of EMIC waves. More importantly, the source regions of EMIC waves caused by two drivers can be clearly distinguished, and the expected high-latitude source region is found during large P_d^+. Our study provides valuable observational evidence to support the two drivers of EMIC wave excitation in the Earth's magnetosphere.

1. Introduction

Electromagnetic ion cyclotron (EMIC) waves are predominantly left handed or weakly linearly polarized waves in the Earth's magnetosphere, typically belonging to Pc1-Pc2 geomagnetic pulsations in the frequency range of 0.1–5 Hz (Anderson et al., 1996; Chen et al., 2019; Cornwall, 1965; Kennel & Petschek, 1966; Min et al., 2012). It is well known that EMIC waves have played an important role in regulating the magnetospheric dynamics, such as ring current decay during the recovery phase of magnetic storm (Thorne & Horne, 1994; Xiao et al., 2011), heavy ion heating (Anderson & Fuselier, 1996; Chen et al., 2018; Horne & Thorne, 1997), and relativistic electron (~MeV) precipitation into upper atmosphere (Ni et al., 2015; Tsurutani et al., 2016; Yuan et al., 2018).

Both theoretical and simulation studies have suggested that there may exist two main potential drivers of EMIC waves in the Earth's magnetosphere: particle injection during substorms (Chen et al., 2014;

Jordanova et al., 2001) and magnetospheric compression due to enhanced solar wind dynamic pressure (McCollough et al., 2012; Olson & Lee, 1983; Zhou & Tsurutani, 1999). In the first scenario, energetic (~10 to 100 keV) protons are injected into the midnight sector of magnetosphere from the magnetotail plasma sheet (~100 eV to 1 keV) during substorms (i.e., large AE), which are unstable to excite EMIC waves in the vicinity of plasmapause or within plasmaspheric plumes during their westward drift (Cornwall, 1965; Fraser et al., 2010). As a result, the main source region of EMIC waves is expected in the dust sector near the magnetic equator, where the dipole magnetic field reaches its minimum (Kennel & Petschek, 1966; Remya et al., 2018). While when the solar wind dynamic pressure (P_d) is significantly enhanced, then the dayside magnetosphere will be compressed, and local remnant energetic (~10 to 100 keV) protons will be betatron accelerated leading to temperature anisotropy and instability (Tsurutani et al., 2002; Zhou & Tsurutani, 1999). The dayside magnetic field will be more flattened, resulting in local magnetic minima at high latitudes (Anderson & Hamilton, 1993; Olson & Lee, 1983). These magnetic minima have been called "minimum B pockets" and are a bifurcation of the magnetic equator (Tsurutani & Smith, 1977). In this case, EMIC waves tend to be excited at relatively higher-latitude regions on the dayside (Jun et al., 2019; Usanova et al., 2012). However, the observational evidence supporting these two scenarios is still required. Although some previous studies have shown the occurrence of EMIC waves is positively correlated with the AE index or P_d parameter (Meredith et al., 2014; Usanova et al., 2012), the role of each driver in exciting waves cannot be distinguished.

In this study, we have developed a new technique to attempt to identify the sources of EMIC wave generation in the Earth's magnetosphere. The effects of storm injection and solar wind dynamic pressure on EMIC waves have been separately investigated with long-term (from September 2012 to December 2017) Van Allen Probes (VAPs) data for the first time. Here, both AE index and P_d parameter have already been modified by considering their time delay. Interestingly, we find that the source region of EMIC waves driven by each driver can be well distinguished, which provides strong observational support for the two expected scenarios of EMIC wave excitation.

2. Data, Instrumentations, and Analysis Method

The VAPs (https://spdf.sci.gsfc.nasa.gov/pub/data/rbsp/), which consist of two identical spacecraft (A and B), are operating in a near-equatorial and highly elliptical orbit with apogee of 5.8 R_E and perigee of 1.1 R_E (Kessel et al., 2012). The Electric and Magnetic Field Instrument Suite and Integrated Science can measure the triaxial magnetic field with 64 samples per second (Kletzing et al., 2013), and the electric field (32 Hz) data are provided by the Electric Field and Waves instrument (Wygant et al., 2013). The satellite position information is obtained by Energetic Particle, Composition, and Thermal Plasma (Spence et al., 2013) Suite, and the corresponding L-shell (L), magnetic local time (MLT), and magnetic latitude (MLAT) values are calculated based on the TS04D model (Tsyganenko & Sitnov, 2005).

The measured magnetic field and electric field data have been converted into mean field-aligned coordinates by the algorithm given in Usanova et al. (2016). The wave's power spectral density is estimated using a fast Fourier transform, whose window width is 4,096 points and sliding step is 512 points. Thus, the frequency and time resolution of magnetic field spectrum are 0.0078 Hz and 8 s, respectively. The parameters for the electric field spectrum are 0.0039 Hz and 16 s, respectively. The data from both probes from September 2012 to December 2017 between L = 3 and 7 are used in this study, and only the waves in the frequency range from f_{cO^+} to f_{cH^+} (where f_{cO^+} and f_{cH^+} denote the gyrofrequencies of O^+ and H^+, respectively) are considered. The total power of each EMIC wave event has been calculated at every time point, and only those with total power greater than 0.01 nT^2/Hz are recorded. To avoid background noises, it is required that each event should last for at least 5 min.

The OMNI geomagnetic index (AE) and solar wind dynamic pressure parameter (P_d) with 1 min resolution (https://omniweb.gsfc.nasa.gov) have been used in this study. Note that the solar wind pressure data, which are provided by the Wind and Ace satellites, have been time shifted to Earth's bow shock nose (King & Papitashvili, 2004).
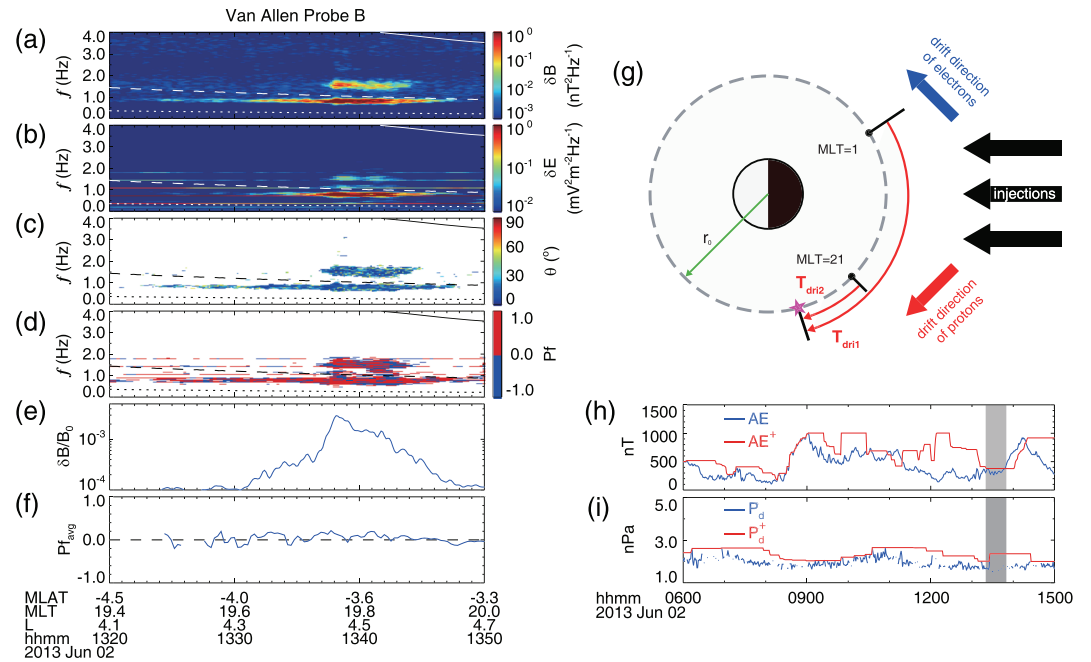
Figure 1. (a–f) The overview of a typical EMIC wave event observed by VAP-B on 2 June 2013, including the spectrogram of total (a) magnetic and (b) electric fields, (c) wave normal angle θ, (d) a flag, "*Pf*," (e) normalized magnetic amplitude $\delta B/B_0$, and (f) power-weighted average *Pf* (Pf_{avg}). In the top four panels, the solid, dashed, and dotted lines represent the local gyrofrequency of proton, helium, and oxygen, respectively. (g) is a diagram showing the method we used to define AE^+ index, and (h) and (i) are the temporal evolution of measured (blue lines) and modified (red line) *AE* index and P_d parameter during 06:00:00 to 15:00:00 on 2 June 2013.

3. Observational Results

Figures 1a–1f present a typical EMIC wave event captured by VAP-B, including the power spectrum density of (a) fluctuating magnetic fields δB and (b) electric fields δE, (c) wave normal angle θ, (d) a flag, "*Pf*," (e) normalized magnetic amplitude $\delta B/B_0$, and (f) power-weighted average *Pf* (i.e., Pf_{avg}). In Figures 1a–1d, the solid, dashed, and dotted lines denote the local proton gyrofrequency f_{cH^+}, helium gyrofrequency f_{cHe^+}, and oxygen gyrofrequency f_{cO^+}, respectively. Here, the wave normal angle and ellipticity are estimated following the method in Means (1972). The flag "*Pf*" (Figure 1d) represents the direction of Poynting vector ($\frac{1}{\mu_0}\overrightarrow{E} \times \overrightarrow{B}$), which equals to either 1.0 (parallel with the background magnetic field) or −1.0 (antiparallel with the background magnetic field). Note that when we calculate "*Pf*," the time points of magnetic field data have been interpolated to those of electric field data. Therefore, the frequency and time resolution of *Pf* are the same with those of electric field spectrum. The magnetic amplitude δB is the root mean square of integration over magnetic power density from f_{cO^+} to f_{cH^+}. We then perform a power-weighted average on *Pf* at each time point to get Pf_{avg}, following Equation 1 in Min et al. (2012). This is a typical EMIC wave event with wave normal angle smaller than 30°. Moreover, this event displays nearly zero Pf_{avg} in this time interval, suggesting a mixture of parallel and antiparallel propagating waves. So we conclude that the spacecraft was in the wave's source region where the instability causes waves to grow and propagate into both directions. This is also a widely used method to determine the source region of EMIC waves in statistical studies (Allen et al., 2015; Loto'aniu et al., 2005).

Since there is usually a time delay between the wave detection and *AE* index or P_d parameter caused by different locations to collect data, then we need to modify them to obtain better proxies of the substorm injection and solar wind compression, that is, AE^+ index and P_d^+ parameter. Figure 1g is a diagram illustrating the substorm injection of energetic (~10 to 100 keV) protons into the midnight sector of magnetosphere (MLT = 21–01: Lopez et al., 1990; Liou et al., 2001). At time T_0 (T_0 represents an arbitrary time point during this time interval), the VAP-B satellite (denoted by the magenta star) is in the dusk sector (MLT₀ ≈ 19.8) at

$L_0 \approx 4.0$. The gradient and curvature drift direction of protons (electrons) is denoted by a red (blue) arrow, and their drift velocity is given by $\overrightarrow{V_{dri}} = \frac{\mu}{q\gamma} \frac{\overrightarrow{b} \times \nabla B}{B} + \frac{p_\parallel^2}{q\gamma m_p} \frac{\overrightarrow{b} \times (\overrightarrow{b} \cdot \nabla) \overrightarrow{b}}{B}$ where q and m_p are the charge and mass of proton and μ, $p_\parallel$, γ, and $\overrightarrow{b}$ represent the magnetic moment, parallel momentum, relativistic factor, and unit vector of the magnetic field, respectively. For simplicity, we assume the background magnetic field is a dipole field. Then the longest drift time T_{dri1}, which means protons drift from MLT = 01 to the position of satellite, can be estimated as $T_{dri1} = \frac{2\pi r_0}{V_{dri}} \times \frac{24 - MLT_0 + 1}{24}$ (where $r_0 = L_0 R_E$). The shortest drift time T_{dri2}, meaning protons drift from MLT = 21 to the satellite, is evaluated as $T_{dri2} = \frac{2\pi r_0}{V_{dri}} \times \frac{24 - MLT_0 - 3}{24}$. Since EMIC waves are commonly believed to be excited by tens of keV protons (Chen et al., 2014; Cornwall, 1965; Usanova et al., 2012), we simply set the averaged kinetic energy of injected protons as $E_k = 25$ keV. Moreover, we might as well assume the pitch angle between proton's velocity and background magnetic field to be 45°. In fact, other pitch angles have also been investigated, but the major results remain unchanged. At last, the AE^+ index is defined as the maximum AE value in the time range from $T_0 - T_{dri1}$ to $T_0 - T_{dri2}$. Note that if MLT_0 is located right in the range of MLT = 21–01, then AE^+ index is estimated as the maximum AE value in the time range from $T_0 - \frac{2\pi r_0}{V_{dri}}$ to T_0, while the P_d^+ parameter is defined as the maximum P_d value in previous 1 hr (Liu et al., 2019), regardless of the satellite's position. For example, the measured (blue lines) and modified (red lines) AE and P_d during 06:00:00–15:00:00 UT on 2 June 2013 are displayed in Figures 1h and 1i, respectively, where the time period of EMIC event in Figures 1a–1f is denoted by the shadows.

To distinguish the role of substorm injection and solar wind compression in exciting EMIC waves, we have investigated how the properties of EMIC waves depend on one index/parameter alone. To do this, we simultaneously restrict the other index/parameter to a very low level. In this study, the EMIC wave events are classified into five AE^+ and P_d^+ categories: low AE^+ and P_d^+ ($AE^+ \leq 100$ nT and $P_d^+ \leq 2$ nPa), low P_d^+ ($P_d^+ \leq 2$ nPa) but moderate AE^+ (100 nT $< AE^+ \leq 300$ nT), low P_d^+ ($P_d^+ \leq 2$ nPa) but strong AE^+ ($AE^+ > 300$ nT), low AE^+ ($AE^+ \leq 100$ nT) but moderate P_d^+ (2 nPa $< P_d^+ \leq 4$ nPa), and low AE^+ ($AE^+ \leq 100$ nT) but strong P_d^+ ($P_d^+ > 4$ nPa). Accordingly, there are 201, 214, 173, 218, and 102 EMIC wave events in each category, and the corresponding observation times are 55.51, 89.21, 56.28, 65.88, and 27.92 hr, respectively.

Figure 2 illustrates the distribution of occurrence rate in the (a–e) L-MLT and (f–j) L-MLAT planes in different categories. The bin sizes in Figures 2a–2e and 2f–2j are 0.5 L × 0.5 MLT and 0.5 L × 3 MLAT, respectively. In Figures 2f–2j, the dashed curves denote the dipole field lines described by $R = L\cos^2(MLAT)$. In each bin, the occurrence rate is defined as the ratio between the total observation time of EMIC waves and the amount of dwell time that VAPs have in the same bin and in the same category. During quiet periods, the occurrence rates of EMIC waves are quite low in the nearly entire L-MLT and L-MLAT planes (Figures 2a and 2f). As the AE^+ increases but the P_d^+ remains low, the occurrence rates of EMIC waves are significantly enhanced in the afternoon and dusk sectors ($13 \leq MLT \leq 20$) at relatively larger L-shells ($5 \leq L \leq 6.5$). Moreover, the waves are preferentially detected near the equator within $|MLAT| < 10°$ (Figures 2g–2h). Unlike substorm injection (i.e., AE^+), with the increase of solar wind pressure P_d^+, there is a clear enhancement of occurrence rate on the dayside ($9 \leq MLT \leq 15$) at $5 \leq L \leq 6.5$. Interestingly, EMIC waves are preferentially observed not only near the magnetic equator but also at relatively higher MLATs ($10° \leq |MLAT| \leq 20°$). Therefore, the EMIC waves induced by two drivers have quite different preferred regions.

We also present the distribution of average normalized amplitude $\delta B/B_0$ in the (a–d) L-MLT and (e–h) L-MLAT planes in Figure 3. Note that the distribution in the quiet times ($AE^+ \leq 100$ nT and $P_d^+ \leq 2$ nPa) is not shown here, due to the very low occurrence rate of waves (Figures 2a and 2f). To reduce statistical error, the bins in which the wave occurrence rate is lower than 1% have been discarded. We found that EMIC waves tend to have larger amplitudes during the period of stronger substorm injection or solar wind dynamic pressure. More interestingly, those strong EMIC waves are preferentially detected just in the regions with high occurrence rates. Under the condition of high AE^+ but low P_d^+ (Figures 3a, 3b, 3e, and 3f), EMIC waves
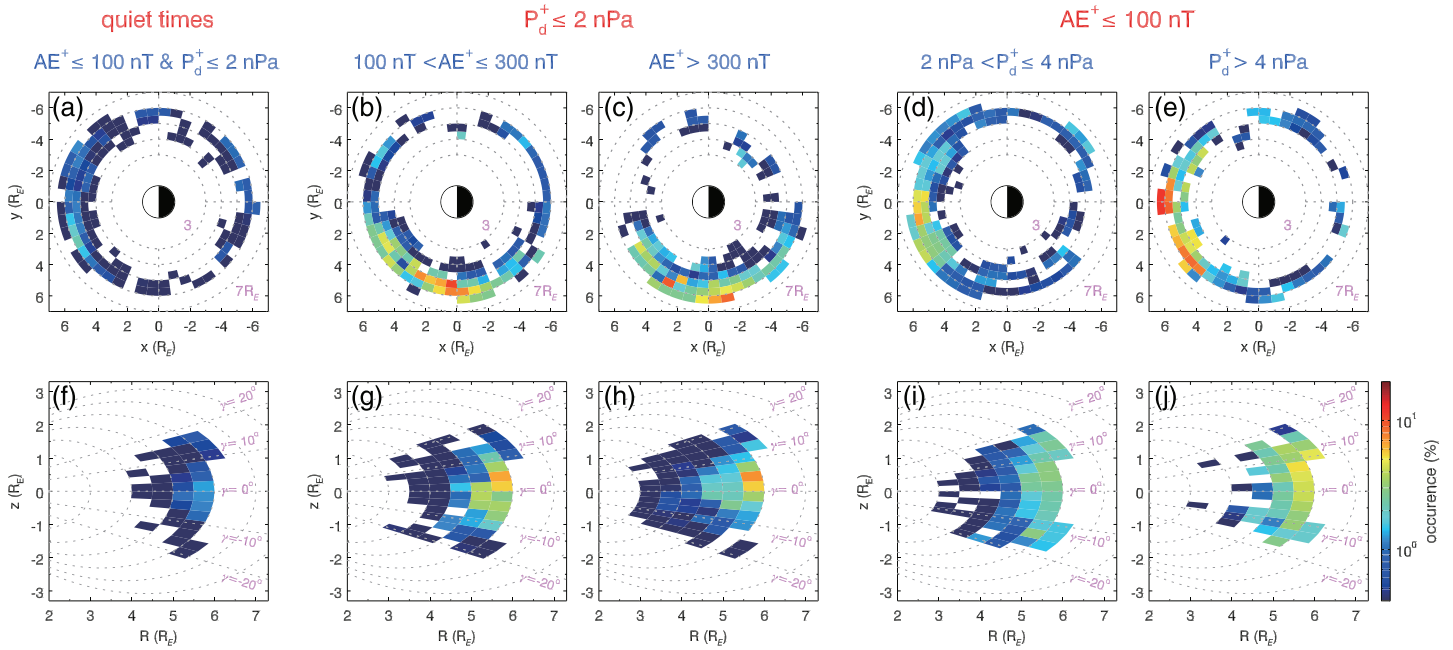
Figure 2. The distribution of wave occurrence rate in the (a–e) L-MLT and (f–j) L-MLAT planes. The columns from left to right correspond to the periods of (a, d) quiet time ($AE^+ \leq 100$ nT and $P_d^+ \leq 2$ nPa), low dynamic pressure ($P_d^+ \leq 2$ nPa) but (b, g) moderate (100 nT $< AE^+ \leq 300$ nT), low dynamic pressure ($P_d^+ \leq 2$ nPa) but (c, h) active geomagnetic activities ($AE^+ > 300$ nT), weak injection ($AE^+ \leq 100$ nT) but (d, i) moderate (2 nPa $< P_d^+ \leq 4$ nPa), and weak injection ($AE^+ \leq 100$ nT) but (e, j) strong solar wind compression ($P_d^+ > 4$ nPa).

having large amplitudes are mainly found in dusk sector near the magnetic equator. While during the period of high P_d^+ but low AE^+, the strong events are mostly distributed in the noon sector at both low and higher MLATs.
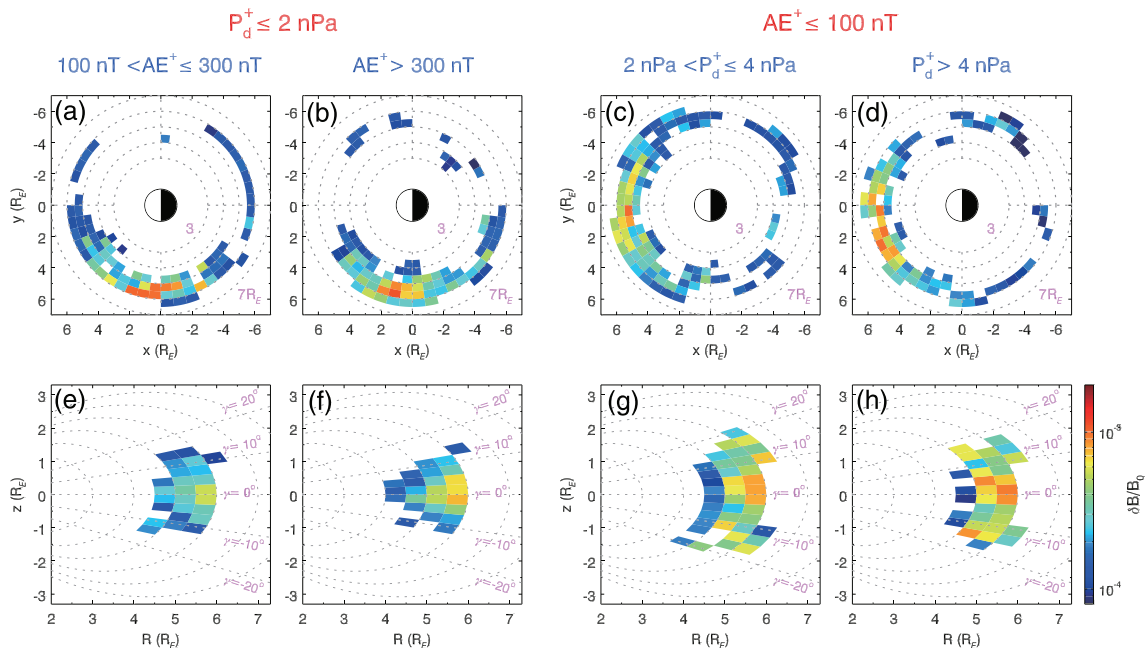

Figure 3. The distribution of average normalized amplitude in the (a–d) L-MLT and (e–h) L-MLAT planes under different conditions.
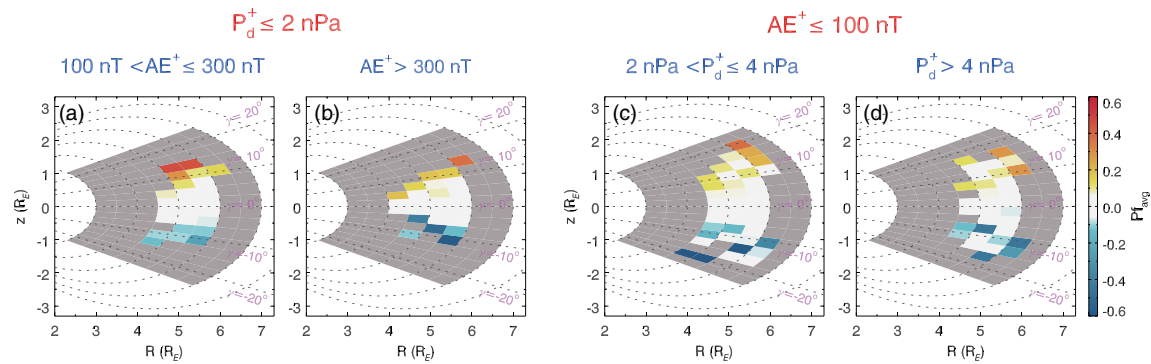
Figure 4. The distribution of average Pf_{avg} in the L-MLAT plane under the condition of low dynamic pressure but (a) moderate and (b) active geomagnetic activities, and weak injection but (c) moderate, and (d) strong solar wind compression.

The source region of EMIC waves induced by each driver is further identified by analyzing the propagating direction of the waves. Figure 4 displays the distribution of average Pf_{avg} value in the L-MLAT planes, where $Pf_{avg} \approx 0$ is considered as the source region of EMIC waves. To make the statistics more convincing, we only consider the bins in which the wave occurrence rate is higher than 1%. During the period of strong AE^+ (Figures 4a and 4b), we find both parallel and antiparallel propagating EMIC waves have essentially the same power, that is, $Pf_{avg} \approx 0$, at relatively lower latitudes ($|MLAT| < 10°$). While at higher latitudes, EMIC waves mainly have only one propagation direction ($|Pf_{avg}| > 0.3$). Therefore, if combined with Figures 2b, 2c, 2g, and 2h, this result indicates that substorm injections lead to the excitation of EMIC wave mainly near the magnetic equator in the dusk sectors. However, when the solar wind dynamic pressure is significantly enhanced, the source region of EMIC waves ($Pf_{avg} \approx 0$) can be found not only near the magnetic equator but also at relatively higher latitudes ($|MLAT| \approx 13°$). This high-latitude source region in minimum B pockets is an expected feature of EMIC waves driven by solar wind dynamic pressure (McCollough et al., 2012; Olson & Lee, 1983; Zhou & Tsurutani, 1999).

4. Discussions and Conclusions

Based on the observations from VAPs during 2012–2017, we have developed a new technique to separately investigate the roles of substorm injection and solar wind dynamic pressure on the excitation of EMIC waves. The time-modified AE^+ and P_d^+ have been used to represent the two drivers in this study. Our statistical results reveal that with the enhancement of either AE^+ or P_d^+, both the occurrence rate and magnetic amplitude of EMIC waves will significantly increase in their source region. However, EMIC waves induced by enhanced substorm injection and solar wind pressure have quite different source regions, which are identified by analyzing the propagating direction of waves. During substorms (high AE^+), EMIC waves are mainly generated in the dusk sector ($16 \leq MLT \leq 20$) and near the magnetic equator ($|MLAT| < 10°$). While during the periods of large solar wind pressure (high P_d^+), the excitation of EMIC waves mainly occurs in the noon sector ($9 \leq MLT \leq 15$), but there are also higher-latitude source regions besides the magnetic equator ($10° < |MLAT| < 20°$).

In the literature, there exist two potential drivers to excite EMIC waves in the Earth's magnetosphere, such as substorm injection (AE) and solar wind dynamic pressure (P_d). On the one hand, during substorms, energetic protons can be injected into the inner magnetosphere from the magnetotail and then drift westward due to the inhomogeneous Earth's magnetic fields. When these energetic protons encounter cold ion populations in dusk sector, it offers an ideal condition for the excitation of EMIC waves, especially near the magnetic equator (Cornwall, 1965; Fraser et al., 2010). This is consistent with our results shown in Figures 4a and 4b, in which EMIC waves are preferentially detected in the dusk sector and near the magnetic equator. On the other hand, the strong solar wind pressure may significantly compress the dayside Earth's magnetosphere and distort its dipole geometry. In this scenario, hot protons will be adiabatically heated in the perpendicular direction, and the high-latitude magnetic minima will also be formed (Anderson & Hamilton, 1993; McCollough et al., 2012; Olson & Lee, 1983). Both effects favor the generation of EMIC waves in the relatively higher-latitude regions. These off-equator source regions have also been confirmed

in our study (Figures 4c and 4d). During quiet time, we can also observe some weak EMIC waves, especially in the postnoon sector. The generation mechanism of these waves is still an open question, which is beyond the scope of this paper and left to further study.

Previous studies have also shown that the occurrence of EMIC waves is positively correlated with AE index or P_d parameter (Jun et al., 2019; Meredith et al., 2014; Usanova et al., 2012). With Combined Release and Radiation Effects Satellite (CRRES) observations, Meredith et al. (2014) showed that the occurrence rate of EMIC waves in the afternoon sector increases during substorms. Usanova et al. (2012) further found that EMIC waves in the dawn sector are preferentially detected when $P_d > 3$ nPa and speculated that these waves may be triggered by the dayside compression of magnetosphere due to the enhanced solar wind pressure. Based on the joint observations from VAP and Geostationary Operational Environment Satellites (GOES) satellites, Jun et al. (2019) also showed that EMIC waves are preferentially observed in the noon sectors when the substorm injections are weak. However, none of them have distinguished the role of each driver in exciting EMIC waves, since the solar wind pressure and substorm injection are usually both enhanced during the active period. In this study, we have separately investigated the effects of substorm injection and solar wind dynamic pressure for the first time by studying the dependence of wave properties on each index/parameter but simultaneously restricting another one to a very low level. In short, our study provides an important insight into the generation mechanism of EMIC waves in the Earth's magnetosphere.

Data Availability Statement

The AE index and solar wind dynamic pressure data were from the OMNI website (https://omniweb.gsfc.nasa.gov). All the data from Van Allen Probes were obtained online (https://spdf.sci.gsfc.nasa.gov/pub/data/rbsp/).

References

Allen, R. C., Zhang, J.-C., Kistler, L. M., Spence, H. E., Lin, R.-L., Klecker, B., et al. (2015). A statistical study of EMIC waves observed by Cluster: 1. Wave properties. *Journal of Geophysical Research: Space Physics*, *120*, 5574–5592. https://doi.org/10.1002/2015JA021333

Anderson, B. J., Denton, R. E., & Fuselier, S. A. (1996). On determining polarization characteristics of ion cyclotron wave magnetic field fluctuations. *Journal of Geophysical Research*, *101*(A6), 13,195–13,213. https://doi.org/10.1029/96JA00633

Anderson, B. J., & Fuselier, S. A. (1996). Response of thermal ions to electromagnetic ion cyclotron waves. *Journal of Geophysical Research*, *99*(A10), 19,413–19,425. https://doi.org/10.1029/94JA01235

Anderson, B. J., & Hamilton, D. J. (1993). Electromagnetic ion cyclotron waves stimulated by modest magnetospheric compressions. *Journal of Geophysical Research*, *98*(A7), 11,369–11,382. https://doi.org/10.1029/93JA00605

Chen, H., Gao, X., Lu, Q., & Wang, S. (2019). Analyzing EMIC waves in the inner magnetosphere using long-term Van Allen Probes observations. *Journal of Geophysical Research: Space Physics*, *124*, 7402–7412. https://doi.org/10.1029/2019JA026965

Chen, H. Y., Gao, X. L., Lu, Q. M., & Wang, S. (2018). In situ observations of harmonic Alfvén waves and associated heavy ion heating. *The Astrophysical Journal*, *859*, 120. https://doi.org/10.3847/1538-4357/aabee2

Chen, L., Jordanova, V. K., Spasojević, M., Thorne, R. M., & Horne, R. B. (2014). Electromagnetic ion cyclotron wave modeling during the geospace environment modeling challenge event. *Journal of Geophysical Research: Space Physics*, *119*, 2963–2977. https://doi.org/10.1002/2013JA019595

Cornwall, J. M. (1965). Cyclotron instabilities and electromagnetic emissions in the ultra low frequency and very low frequency ranges. *Journal of Geophysical Research*, *70*(1), 61–69. https://doi.org/10.1029/JZ070i001p00061

Fraser, B. J., Grew, R. S., Morley, S. K., Green, J. C., Singer, H. J., Loto'aniu, T. M., & Thomsen, M. F. (2010). Storm time observations of electromagnetic ion cyclotron waves at geosynchronous orbit: GOES results. *Journal of Geophysical Research*, *115*, A05208. https://doi.org/10.1029/2009JA014516

Horne, R. B., & Thorne, R. M. (1997). Wave heating of He$^+$ by electromagnetic ion cyclotron waves in the magnetosphere: Heating near the H$^+$-He$^+$ bi-ion resonance frequency. *Journal of Geophysical Research*, *102*(A6), 11,457–11,471. https://doi.org/10.1029/97JA00749

Jordanova, V., Farrugia, C., Thorne, R., Khazanov, G. V., Reeves, G., & Thomsen, M. (2001). Modeling ring current proton precipitation by EMIC waves during the May 14-16, 1997, storm. *Journal of Geophysical Research*, *106*(A1), 7–22. https://doi.org/10.1029/2000JA002008

Jun, C.-W., Yue, C., Bortnik, J., Lyons, L. R., Nishimura, Y. T., Kletzing, C. A., et al. (2019). A statistical study of EMIC waves associated with and without energetic particle injection from the magnetotail. *Journal of Geophysical Research: Space Physics*, *124*, 433–450. https://doi.org/10.1029/2018JA025886

Kennel, C. F., & Petschek, H. E. (1966). Limit on stably trapped particle fluxes. *Journal of Geophysical Research*, *71*(1), 1–28. https://doi.org/10.1029/JZ071i001p00001

Kessel, R. L., Fox, N. J., & Weiss, M. (2012). The radiation belt storm probes (RBSP) and space weather. *Space Science Reviews*, *179*(1–4), 531–543. https://doi.org/10.1007/s11214-012-9953-6

King, J. H., & Papitashvili, N. E. (2004). Solar wind spatial scales in and comparisons of hourly Wind and ACE plasma and magnetic field data. *Journal of Geophysical Research*, *110*, A02209. https://doi.org/10.1029/2004JA010804

Kletzing, C. A., Kurth, W. S., Acuna, M., MacDowall, R. J., Torbert, R. B., Averkamp, T., et al. (2013). The Electric and Magnetic Field Instrument Suite and Integrated Science (EMFISIS) on RBSP. *Space Science Reviews*, *179*(1–4), 127–181. https://doi.org/10.1007/s11214-013-9993-6

Liou, K., Meng, C.-I., Newell, P. T., Lui, A. T. Y., Reeves, G. D., & Belian, R. D. (2001). Particle injections with auroral expansions. *Journal of Geophysical Research*, *106*(A4), 5873–5881. https://doi.org/10.1029/2000ja003003

Liu, S., Xia, Z., Chen, L., Liu, Y., Liao, Z., & Zhu, H. (2019). Magnetospheric Multiscale Observation of quasiperiodic EMIC waves associated with enhanced solar wind pressure. *Geophysical Research Letters*, *46*, 7096–7104. https://doi.org/10.1029/2019GL083421

Lopez, R. E., Sibeck, D. G., McEntire, R. W., & Krimigis, S. M. (1990). The energetic ion substorm injection boundary. *Journal of Geophysical Research*, *95*(A1), 109–117. https://doi.org/10.1029/ja095ia01p00109

Loto'aniu, T. M., Fraser, B. J., & Waters, C. L. (2005). Propagation of electromagnetic ion cyclotron wave energy in the magnetosphere. *Journal of Geophysical Research*, *110*, A07214. https://doi.org/10.1029/2004JA010816

McCollough, J. P., Elkington, S. R., & Baker, D. N. (2012). The role of Shabansky orbits in compression-related electromagnetic ion cyclotron wave growth. *Journal of Geophysical Research*, *117*, A01208. https://doi.org/10.1029/2011JA016948

Means, J. D. (1972). Use of the three-dimensional covariance matrix in analyzing the polarization properties of plane waves. *Journal of Geophysical Research*, *77*(28), 5551–5559. https://doi.org/10.1029/JA077i028p05551

Meredith, N. P., Horne, R. B., Kersten, T., Fraser, B. J., & Grew, R. S. (2014). Global morphology and spectral properties of EMIC waves derived from CRRES observations. *Journal of Geophysical Research: Space Physics*, *119*, 5328–5342. https://doi.org/10.1002/2014JA020064

Min, K., Lee, J., Keika, K., & Li, W. (2012). Global distribution of EMIC waves derived from THEMIS observations. *Journal of Geophysical Research*, *117*, A05219. https://doi.org/10.1029/2012JA017515

Ni, B., Cao, X., Zou, Z., Zhou, C., Gu, X., Bortnik, J., et al. (2015). Resonant scattering of outer zone relativistic electrons by multiband EMIC waves and resultant electron loss time scales. *Journal of Geophysical Research: Space Physics*, *120*, 7357–7373. https://doi.org/10.1002/2015JA021466

Olson, J. V., & Lee, L. C. (1983). Pc1 wave generation by sudden impulses. *Planetary and Space Science*, *31*(3), 295–302. https://doi.org/10.1016/0032-0633(83)90079-X

Remya, B., Sibeck, D. G., Halford, A. J., Murphy, K. R., Reeves, G. D., Singer, H. J., et al. (2018). Ion injection triggered EMIC waves in the Earth's magnetosphere. *Journal of Geophysical Research: Space Physics*, *123*, 4921–4938. https://doi.org/10.1029/2018JA025354

Spence, H. E., Reeves, G. D., Baker, D. N., Blake, J. B., Bolton, M., Bourdarie, S., et al. (2013). Science goals and overview of the radiation belt storm probes (RBSP) energetic particle, composition, and thermal plasma (ECT) suite on NASA's Van Allen Probes Mission. *Space Science Reviews*, *179*(1–4), 311–336. https://doi.org/10.1007/s11214-013-0007-5

Thorne, R. M., & Horne, R. B. (1994). Energy transfer between energetic ring current H^+ and O^+ by electromagnetic ion cyclotron waves. *Journal of Geophysical Research*, *99*(A9), 17,275–17,282. https://doi.org/10.1029/94JA01007

Tsurutani, B. T., Arballo, J. K., Zhou, X.-Y., Galvan, C., & Chao, J. K. (2002). Electromagnetic electron and proton cyclotron waves in geospace: A Cassini snapshot. In L.-H. Lyu (Ed.), *Space weather study using multipoint techniques* (pp. 97–125). Elsevier Science Ltd: Pergamon.

Tsurutani, B. T., Hajra, R., Tanimori, T., Takada, A., Remya, B., Mannucci, A. J., et al. (2016). Heliospheric plasma sheet (HPS) impingement onto the magnetosphere as a cause of relativistic electron dropouts (REDs) via coherent EMIC wave scattering with possible consequences for climate change mechanisms. *Journal of Geophysical Research: Space Physics*, *121*, 10,130–10,156. https://doi.org/10.1002/2016JA022499

Tsurutani, B. T., & Smith, E. J. (1977). Two types of magnetospheric ELF chorus and their substorm dependences. *Journal of Geophysical Research*, *82*(32), 5112–5128. https://doi.org/10.1029/JA082i032p05112

Tsyganenko, N. A., & Sitnov, M. I. (2005). Modeling the dynamics of the inner magnetosphere during strong geomagnetic storms. *Journal of Geophysical Research*, *110*, A03208. https://doi.org/10.1029/2004JA010798

Usanova, M. E., Malaspina, D. M., Jaynes, A. N., Bruder, R. J., Mann, I. R., Wygant, J. R., & Ergun, R. E. (2016). Van Allen Probes observations of oxygen cyclotron harmonic waves in the inner magnetosphere. *Geophysical Research Letters*, *43*, 8827–8834. https://doi.org/10.1002/2016GL070233

Usanova, M. E., Mann, I. R., Bortnik, J., Shao, L., & Angelopoulos, V. (2012). THEMIS observations of electromagnetic ion cyclotron wave occurrence: Dependence on AE, SYMH, and solar wind dynamic pressure. *Journal of Geophysical Research*, *117*, A10218. https://doi.org/10.1029/2012JA018049

Wygant, J. R., Bonnell, J. W., Goetz, K., Ergun, R. E., Mozer, F. S., Bale, S. D., et al. (2013). The electric field and waves instruments on the radiation belt storm probes mission. *Space Science Reviews*, *179*(1–4), 183–220. https://doi.org/10.1007/s11214-013-0013-7

Xiao, F. L., Chen, L. X., He, Y. H., Su, Z. P., & Zheng, H. N. (2011). Modeling for precipitation loss of ring current protons by electromagnetic ion cyclotron waves. *Journal of Atmospheric and Solar - Terrestrial Physics*, *73*(1), 106–111. https://doi.org/10.1016/j.jastp.2010.01.007

Yuan, Z., Liu, K., Yu, X., Yao, F., Huang, S., Wang, D., & Ouyang, Z. (2018). Precipitation of radiation belt electrons by EMIC waves with conjugated observations of NOAA and Van Allen satellites. *Geophysical Research Letters*, *45*, 12,694–12,702. https://doi.org/10.1029/2018GL080481

Zhou, X., & Tsurutani, B. T. (1999). Rapid intensification and propagation of the dayside aurora: Large scale interplanetary pressure pulses (fast shocks). *Geophysical Research Letters*, *26*(8), 1097–1100. https://doi.org/10.1029/1999GL900173